Spatial and Spectral Super-Resolution Imaging for Characterizing Multi-Chromophoric Systems

Hyung Jun Kim, Youngah Kwon, Han Yang, Alexander J. Devanny, and Laura J. Kaufman* Department of Chemistry, Columbia University, New York, New York 10027, United States

*corresponding author: kaufman@chem.columbia.edu

ABSTRACT

We demonstrate simultaneous spatial and spectral subtraction-based super-resolution microscopy based on photobleaching, photoblinking, or photoactivation in multi-chromophoric systems to detail characteristics of individual emitters in small aggregates isolated and immobilized in polymeric films. In particular, we investigate the prototypical multi-chromophoric electron donating system poly[2-methoxy-5-(2-ethylhexyloxy)-1,4-phenylenevinylene] (MEH-PPV) as well as electron accepting N,N'-dipentyl-3,4,9,10-perylenedicarboximide (pPDI) molecules prepared as small aggregates via tandem analysis of spatial and spectral information of individual emitters within a diffraction-limited spot. In MEH-PPV aggregates, this approach reveals evidence of both chain-limited and domain-limited exciton migration as well as preferential photodegradation of regions with a high number of intermolecular contacts. In small aggregates of pPDI, evidence of individual subunits with distinct spectral characteristics and electronic coupling properties is found.

Introduction

Recent advances in optical fluorescence microscopy present opportunities to improve understanding of morphological and photophysical properties of molecules of interest for use in a variety of optoelectronic applications^{1,2}. Such molecules typically have endogenous chromophores, such that far-field optical approaches can be employed, thus avoiding challenges associated with other high resolution imaging techniques including electron microscopy and scanning probe microscopy, techniques that are time-consuming, are restricted to small imaging areas, and may require perturbative sample preparation^{3,4}. Furthermore, optical approaches can yield information on correlations between conformation and photophysical properties as well as heterogeneity of these properties^{5,6}. Despite such advantages, there are challenges associated with using the intrinsic photoluminescence of molecules to understand molecular conformation, photophysics, and correlation between these properties, particularly in multi-chromophoric systems where multiple emitters exist within a diffraction limited spot and where interactions between chromophores may lead to quenching or spectral shifts that alter intensity and/or prevent direct detection⁷. Here, we show how use of a spatial and spectral subtraction-based superresolution microscopy using photobleaching, photoblinking, or photoactivation of intrinsic emitters in systems with multiple chromophores within a diffraction-limited spot yields new insight into properties of individual emitters.

As proof of principle, we study two prototypical systems of interest in organic optoelectronic devices, poly[2-methoxy-5-(2-ethylhexyloxy)-1,4-phenylenevinylene] (MEH-PPV) and N,N'-dipentyl-3,4,9,10-perylenedicarboximide (pPDI). Polyphenylene vinylenes are representative conjugated polymers that may serve as electron donors and hole transporting materials^{8,9}. Similarly, PDI derivatives have been extensively investigated as potential electron

acceptors¹⁰. In both cases, these classes of molecules are of interest for their tunable exciton bands as dictated by particular substituents as well as by intermolecular interactions that affect their electronic coupling and resultant photophysics^{11,12}. Indeed, in solid state devices the properties of these molecules are set largely by their conformation. For MEH-PPV and similar molecules, this is evident even at the single molecule level, as these molecules are multi-chromophoric in absorption and emission. Such properties have been extensively studied at the single molecule level and to a certain extent in aggregates that more fully recapitulate intermolecular interactions present in devices^{1,13–15}. For PDI derivatives, particular molecular and supramolecular structure also strongly dictate photophysical behavior, with large scale fibrillar structures showing particular promise for electron transport^{16–18}.

In an effort to enhance physical understanding of multi-chromophoric and supramolecular structures, super-resolution imaging methods have been developed that take advantage of stochastic inherent or induced photoactivation, transient binding, blinking or bleaching^{19–24}. Herein, we use such an approach incorporating concurrent spatial and spectral super-resolution imaging to characterize individual emitters on small aggregates of MEH-PPV and pPDI. While many researchers have studied aspects of these molecules or aggregates thereof to characterize and understand correlations between molecular conformation and photophysical properties, few have done so with resolution beyond the diffraction limit, which can provide insight into individual emitter properties within these systems. Vacha and co-workers first brought localization microscopy to bear on MEH-PPV, showing that centroid position varied over time, tracking the center of mass of emitters and tracing out conformation of the molecules²⁵. In earlier work, Rothberg and co-workers monitored fluorescence spectra of single MEH-PPV molecules over time, in essence performing a spectral version of the approach demonstrated by Vacha, showing

that typical molecule emission shifted to the blue over the course of photodegradation and photobleaching²⁶, and Yu et al. used spectral subtraction to provide evidence of efficient energy transfer in collapsed regions of MEH-PPV molecules²⁷. Park et al. used a super-resolution technique predicated on serial emitter photobleaching to locate the position of each emitter and trace out individual MEH-PPV molecular conformation²². Jiang et al. used localization imaging together with spectral subtractions to characterize emitters quenched by polarons in the conjugated polymer F8BT²⁸.

Here, we perform simultaneous subtraction-based super-resolution localization and spectroscopy on aggregates of MEH-PPV and pPDI to directly address each emitter in the assembled structure and their corresponding photophysical behaviors. This dual subtraction-based approach reveals that MEH-PPV prepared as small aggregates shows emission that shifts towards higher energy over the course of photodegradation, with evidence of both chain- and domain-limited exciton migration. Applying the multi-dimensional super-resolution technique to pPDI assemblies reveals individual subunits with spectral characteristics consistent with distinct electronic coupling properties.

Experimental Details

Sample Preparation. MEH-PPV (Mw = 252 kDa with PDI = 1.8) was purchased from Polymer Source. pPDI was purchased from Sigma-Aldrich. Both were dissolved in toluene to prepare a stock solution. Polystyrene (PS) (P4250-S, Polymer Source, Mw= 168 kDa, PDI= 1.05) stock solutions were re-precipitated in hexane 3 times and dissolved in toluene. This solution was then photobleached at 533 nm for \approx 48 hours to eliminate fluorescence from impurities. For all experiments, probes were diluted in \approx 3.5 wt% polystyrene with toluene as the solvent. The

solutions were spin coat onto a glass coverslip at 3000 rpm, resulting in a film of \approx 180 nm thickness. Sample films were prepared such that isolated fluorescent features were present at a density of \approx 0.3 spots/ μ m² for MEH-PPV and \approx 0.2 spots/ μ m² for pPDI. Films were exposed to nitrogen gas flow for \approx 60 min to remove residual solvent. In some cases, solvent vapor swelling was then applied to induce a small degree of aggregation²⁹. In those cases, a mixture of acetone and chloroform solvent with 50:50 liquid volume ratio was applied to swell the film from the initial thickness \approx 180 nm to \approx 300 nm for 20 min. Swollen samples were then again exposed to nitrogen gas flow for \approx 60 min to de-swell and assist with removal of residual solvent, a procedure that has previously been shown to return film thickness to that measured before solvent swelling¹⁵. All experiments were conducted at room temperature (\approx 21 °C).

Experimental Setup. All imaging experiments were performed on a wide-field fluorescence microscope on an inverted microscope body (IX71, Olympus), as depicted schematically in Fig. 1. A 532 nm continuous-wave laser (LRS-532-TM-30-5, Laserglow Technologies) was used as the excitation source. Excitation light was passed through a dichroic mirror (DI-03-R405/488/532/635-T1-25X36, Semrock) and focused onto the back-focal plane of an oil-immersion objective (UAPON 1000TIRF NA 1.49, Olympus) to achieve wide field illumination. Samples were illuminated at a power density of ≈ 150 W/cm² for MEH-PPV and ≈ 300 W/cm² for pPDI. Fluorescence was collected by the same objective and filtered using a long-pass filter (LP03-532RU, Semrock). To simultaneously collect spatial and spectral information, a transmission grating (GT13-03 300 grooves/mm 17.5° groove angle, Thorlabs) was mounted in front of the EM-CCD camera (iXon DV885 KCS-VP, Andor). The position and orientation of the grating was set such that the spatial (spectral) domain information was located on the left (right) side of the EM-CCD without spatial overlap (Fig. 1). In the current implementation, counts per pixel in the first-

order image are approximately 2 times greater than in the zeroth-order image. Data was collected at frame rates ranging from 0.2 - 1.0 s with EM gain ranging from 80 to 150 over a customized pixel area of 1002 pixels x 401 pixels for efficient CCD cooling and data processing. For assessment of spatial localization error, counts were converted to photons via a function consisting of CCD settings and parameters including EM gain and quantum efficiency.

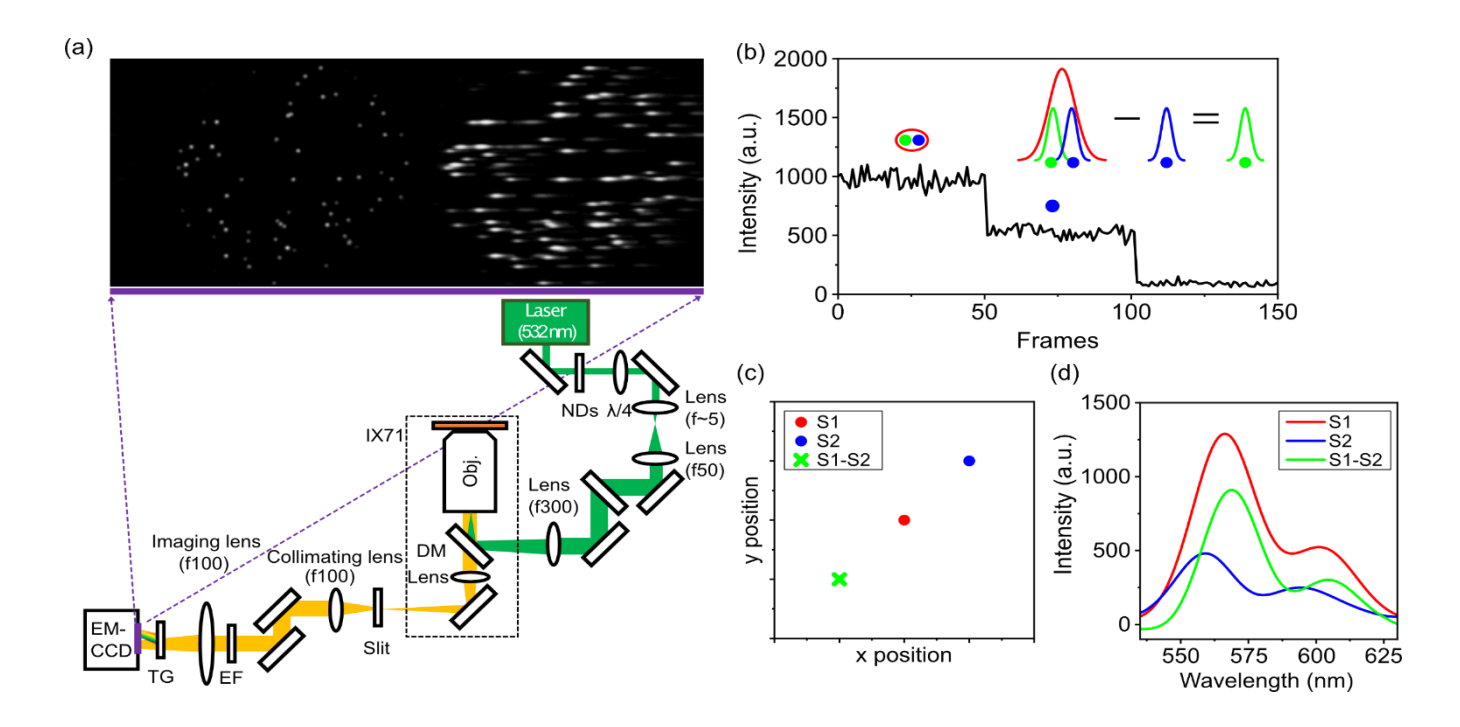


Figure 1. (a) Experimental setup and a representative image of zeroth- and first-order data on the left and right sides of the EM-CCD, respectively. NDs, neutral density filters; $\lambda/4$, quarter-wave plate; DM, dichroic mirror; Obj, objective; EF, emission filter; TG, transmission grating. (b) Schematic depiction of the experimental approach: from the zeroth-order image, a fluorescence intensity trajectory is obtained; in this example, two emitting sites that sequentially photobleach are evident. The initial feature has contributions from both the green and blue emitting sites, and subtraction reveals information about the green emitting site. (c) Schematic depiction of positions obtained from performing localization microscopy (red and blue circles) as well as that obtained via afSHRImP (green cross). (d) Schematic depiction of the corresponding fluorescence spectra obtained from the first-order data for each section shown in (b) as well as the spectrum obtained by subtracting the spectrum in Section 2 from that in Section 1 (S1-S2, green).

Results and Discussion

Spectral Calibration

For calibration of the spectral portion of the data, TetraSpeck beads (100 nm; emission peaks: 430/515/580/680 nm, T7279, Invitrogen) were employed. First, an ensemble spectrum of the beads in solution was measured to establish the spectral peak positions to the red of the excitation line, with identified peaks at 581.5 and 675.5 nm (Fig. S1a). Then, beads were deposited onto a poly-L-lysine coated coverslip and were imaged on the wide-field microscope. Emission was collected for 50 frames with 200 ms exposure time, and movies were exported to ImageJ for analysis. Following generation of a three frame-averaged movie as described in Reference 22, smoothing and background subtraction were performed. Such data processing is required due to the noise associated with the high EM gain used, which is necessary to attain sufficient intensity in both the zeroth- and first-order modes. Smoothing was performed via an ImageJ function that replaces intensity at each pixel with the average of pixels in its 3x3 neighborhood to mitigate noise as well as to account for the fact that the imaged spectrum may span more than a single pixel in the y dimension. Following this, background subtraction using a rolling ball algorithm with a ball radius of 10 pixels was performed. Single pixel line profiles, chosen by selecting the line with maximum photon counts among the several line profiles associated with a single bead, were plotted (Fig. S1b). Emission peak positions were identified as pixels displaying maximum local intensity. From these measurements, pixel to wavelength conversion was formulated as

$$\lambda = 1.175(x - (x_0 + D)) + 581.5 \tag{1}$$

where x is position in pixels, x_0 is the zeroth-order centroid position of the feature in pixels, and D is the distance in pixels between the centroid position of the feature in the zeroth-order image and

the first peak of the spectrum. Using this conversion, apparent spectral heterogeneity of the TetraSpeck beads was evaluated. First, the time-dependence of the first spectral peak of a particular bead over 50 200ms frames was assessed. This revealed high apparent spectral stability, with the peak at 582 ± 1 nm and no trend over time (Fig. S1c,d). Then, variation across beads was investigated (Fig. S1e,f). Over 23 beads, this also yielded peak position of 582 ± 1 nm, and no apparent dependence on position, suggesting no effect of spherical or related aberrations on apparent wavelength. Given the high spectral stability across time and beads revealed by the calibration with Tetraspeck beads, we use Equation 1 for all further pixel to wavelength conversion in this work.

Single Emitter Validation

Following spectral calibration, localization and spectral precision were established from measurements on single pPDI molecules, all of which displayed similar intensity and had single step photobleaching behavior. In contrast to implementation of super-resolution imaging based on photobleaching demonstrated previously²², for combined imaging and spectroscopy, data smoothing and background associated with the presence of the transmission grating was performed on the three frame-averaged movie (1 s per frame before averaging for this data set), as described in the spectral calibration section above.

To assess uncertainty in position of individual identified emitters, 2D Gaussian fitting with a Levenberg Marquadt algorithm was used and parameter fit uncertainty $\delta r = \frac{1}{2}(\delta x + \delta y)$ was determined via the parameter covariance matrix. This measure has previously been reported to yield similar results to that estimated from experimental parameters¹⁹. We investigated whether this was the case for measurements on 19 single pPDI molecules, which have more similar signal

levels to the small aggregates evaluated in this study than do Tetraspeck beads. Fit uncertainty as determined from 2D Gaussian fitting was plot vs. photons collected in a given frame (Fig. S2a) and compared to a theoretical prediction for localization error via $(\sigma_i = \left(\frac{s^2 + a^2/12}{N} + \frac{8\pi s^4 b^2}{a^2 N^2}\right)^{1/2})$ with σ_i the localization error along x or y, s the standard deviation of the point spread function (114 nm for our experimental setup), a the size of the pixel (90 nm), N the number of photons collected from the emitter in a single frame, and b the background photons per pixel, for which we use the residual background averaged value after background subtraction (b = 3.3)³⁰. While the trend in fit uncertainty vs. number of photons generally follows the theoretical prediction, uncertainty assessed through fitting overestimates fit uncertainty relative to the prediction for low photon counts and underestimates the quantity at higher photon counts. Evaluating localization error directly from the standard deviation of localizations of each pPDI molecule assessed vs. average number of photons per frame for each molecule yields localization error quite similar to the theoretical prediction (Fig. S2b,c). The overall consistency with the theoretical prediction suggests not only that background subtraction does not strongly affect localization error but also that drift is not a significant source of localization error in this study. The finding on drift is further supported by drift assessment studies (Fig. S3), and data is not de-drifted in this study.

As for the TetraSpeck beads, we also evaluated apparent spectral heterogeneity of single pPDI molecules over time as well as across molecules (Fig. S4). Spectra from the same 19 single pPDI molecules assessed for localization error are shown in Fig. S4a. We note that only a portion of the 0-0 vibronic band is evident due to the dichroic mirror employed in this study, and thus we focus on the 0-1 vibronic band. The spectral stability of a representative molecule is shown in Fig. S4b,c. This revealed high spectral stability, with the maximum value of the 0-1 peak centered at

 582 ± 1 nm over 180 frames, with no trend over time. The standard deviation, which is somewhat higher than for the Tetraspeck beads, is consistent with the lower signal to background ratio present for these single molecules compared to the bead sample. As for the beads, we also compared peak position across pPDI molecules, revealing the peak of the 0-1 vibronic band to be 581 ± 3 nm, with no trend as a function of distance from the center of the zeroth-order image (Fig. S4d,e).

Case Study 1: MEH-PPV Features with Few Emitters

Given the high localization and spectral precision obtained from single pPDI molecules, we conclude that the multi-dimensional approach is feasible. However, to provide spatial and spectral information on individual emitters within a diffraction limited spot, clarifying precision of spatial and spectral information obtained following the subtractions shown schematically in Fig. 1 is also necessary. To that end, we provide a case study on a single MEH-PPV feature that shows two-step photobleaching behavior, consistent with the presence of two emitting units on a single molecule or small aggregate, as schematically depicted in Fig. 1.

For the subtraction-based approach shown in Fig. 1, we employ all-frames single molecule high resolution imaging with photobleaching (afSHRImP) as reported in Reference 22. Briefly, every pair of frames in the three-frame average intensity trajectory is subjected to subtraction. 2D Gaussian fitting is performed on each resulting image, and localization uncertainty and eccentricity of the resulting fits are displayed in a matrix. From this matrix, visual inspection allows identification of sections for further analysis, with sectioning additionally validated by performing fast Step Transition and State Identification (STaSI), which identifies states and interstate step transitions from discrete fluorescence intensity trajectory data³¹.

Data from an exemplary MEH-PPV feature in which two-step bleaching occurs is shown in Fig. 2. First, frame-by-frame localization analysis was performed (small symbols in Fig. 2b). Then, frame-subtractions were undertaken, and the full arrays of resulting fit uncertainties and eccentricities are shown in Fig. S5. Subtracted images between frame pairs were considered to be associated with photophysical events (photobleaching in this case) when the resulting image could be fit to a 2D Gaussian with fit uncertainty ≤ 0.10 pixels (9 nm) and eccentricity ≤ 0.65 , where eccentricity, e, is given by $e = (1 - (l^2/L^2))^{1/2}$, with L the semi-major axis and l is the semi-minor axis of the fit Gaussian²².

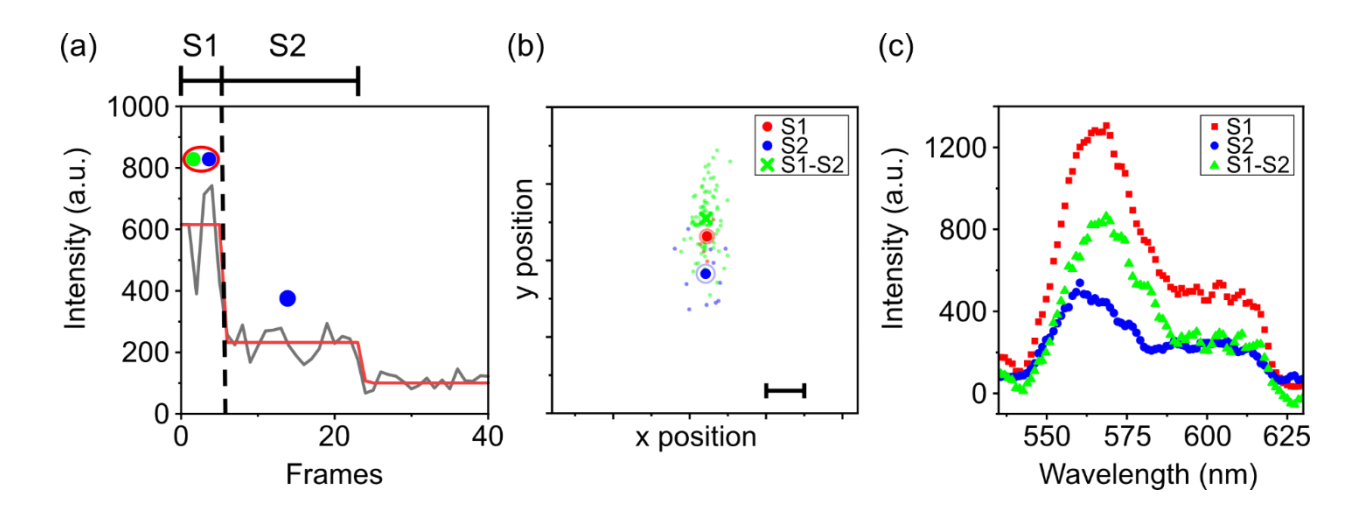


Figure 2. Case study of an MEH-PPV feature with two emitting sites. (a) Fluorescence intensity trajectory plotted from a single pixel associated with the feature (gray) shows a two-step decay, with analyzed sections labeled S1 and S2 and a schematic depiction of emitters present in each section. Red line indicates intensity as identified by STaSI. (b) Frame-by-frame localizations (small points) and weight-averaged localizations of the imaged feature present in S1 (red) and S2 (blue) as well as first bleached emitter position obtained from afSHRImP (green cross). Circles represent the standard error of points identified from localization (S1, S2) or afSHRImP (S1-S2) imaging. Scale bar: 22.5 nm. (c) Corresponding spectra obtained by averaging all spectra collected during S1 (red), S2 (blue), and via subtraction (green).

For the exemplary feature associated with the data in Fig. 2 and Fig. S5, there is an obvious intensity decrease that occurs around the fifth frame of the trajectory. This corresponds to the region of low fit uncertainty and eccentricity that can be seen in the afSHRImP matrix (blue pixels,

Fig. S5a,b). We select the frame associated with the end of a section (S1 in this case) by identifying the frame at which nearly all combinations with previous frames result in fits with low uncertainty and eccentricity (in this case, frame 5). As a check for this identification, we perform STaSI, which also identifies the relevant frame as frame 5. All combinations of frames in S1 and S2 whose subtractions satisfy the localization and uncertainty constraints detailed above are, following weight averaging by fit uncertainty, used to identify the position associated with the emitter only emitting in S1. All localizations performed on data in S2 are similarly weight-averaged by fit uncertainty to determine the position of the emitter in S2. Because localizations within particular sections can be averaged, the effective number of photons is greater than that associated with a single frame and the standard error of the mean is decreased relative to the localization error assessed through a single frame. This is shown in Fig. S6 for the sections and afSHRImP analysis associated with the data in Fig. 2. Fig. S6 also includes data from other MEH-PPV and pPDI features analyzed analogously in this manuscript (vide infra). As shown for pPDI single molecules in Fig. S2c, localization error found empirically for identified features in Fig. S2 is quite similar to the theoretical prediction, and the ability to average over sections or afSHRImP points greatly reduces error relative to that associated with a single frame.

In the technique we term spectral SHRImP, spectra from frames associated with S1 (S2) are averaged to produce the red (blue) spectrum in Fig. 2, with the green spectrum associated with the emitter on only in S1 identified through subtraction of the blue from red spectrum. As expected, the distance between emitters identified by afSHRImP is greater than that determined by localization imaging, which averages over emitter positions if more than one is present. For the same reason, the spectrum of the first emitter to turn off as revealed by subtraction is more different than (and more red-shifted than) the spectrum of the second emitter than is the spectrum associated

with S1, which has contributions from both emitters. This is consistent with previous measurements that show MEH-PPV emission tends to shift blue over time^{26,32,33}.

This intriguing finding led us to investigate additional MEH-PPV features with one and two-step photobleaching behavior via the combined spatial and spectral subtraction-based superresolution technique described above. We note that given the initial concentration of MEH-PPV molecules and degree and time of swelling as described in the Experimental Details, previous work suggests typical MEH-PPV aggregates in this study are composed of fewer than 40 single molecules and extend less than 100 x 40 nm^{15,34}. Twenty-three features with two or three step photobleaching were studied. In all cases, sectioning was performed via STaSI; the characteristics of the final surviving emitter were determined through localization imaging and averaging the spectra of all frames associated with the final section, and the characteristics of the first and/or second emitters to photobleach were determined via afSHRImP subtractions for spatial information and spectral averaging and subtraction for spectral information, both as described above. Spectra were fit to two Gaussians to determine emission peaks and peak heights of the 0-0 and 0-1 vibronic bands. This analysis revealed that behavior seen in the molecule depicted in Fig. 2 is representative: the 0-0 peak position shifts towards the blue (Fig. 3a) and the 0-0/0-1 peak ratio decreases (Fig. 3b) for emitters that survive photobleaching longest. The tendency for MEH-PPV fluorescence to shift towards the blue upon extended excitation and partial photobleaching has been noted previously both via direct spectral measurements^{26,32} and as inferred from polarization modulation measurements³⁵. The blue shift in emission upon extended exposure to excitation light has been proposed to be a consequence of efficient energy funneling to highly ordered, tightly packed domains, which in turn are prone to photochemical defects and efficient photobleaching due to the long residence time of excitation in these domains. The highly ordered,

tightly packed domains are the most red-lying states and are traditionally associated with a high number of intermolecular contacts and long conjugation lengths, which are consistent with larger 0-0/0-1 ratios^{32,36}. As a result, over time the emission spectrum shifts both towards the blue and towards exhibiting lower 0-0/0-1 peak ratios. This work directly confirms that photobleaching events occur preferentially in domains with particular spectral character consistent with ordered, tightly packed domains.

Additionally, to highlight the utility of the multi-dimensional approach based on spatial and spectral subtractions, we investigated whether spatial and spectral characteristics of emitters and spectral and spatial changes that occurred upon serial emitter photobleaching were correlated. In particular, distance between emitters, intensity change, spectral shift of the 0-0 peak, and change in 0-0/0-1 ratio upon serial photobleaching events were investigated. Generally, correlations between spatial, intensity, and spectral information were weak. Fig. S7, for example, shows 0-0 peak position of identified emitters vs. position relative to the center of mass of emission as well as vs. distance between emitting sites, and Fig. S8 shows shift in 0-0 peak position vs. distance between emitting sites. In Fig. S7b and S8, these quantities are identified with the dual subtraction technique as well as via the simpler technique that monitors spectral peak and centroid position over time without subtractions. While the subtraction-based technique shows greater degree of distance between emitters and difference in peak position than the subtraction-free technique, neither approach suggests strong correlation in these quantities. In contrast, notable correlation was found between spectral shift of the 0-0 peak and intensity change associated with a photobleaching event, and this correlation was made more obvious by applying the subtractionbased technique vs. the simpler temporal evolution technique (Fig. 3c, Fig. S9). In particular, large spectral shifts were found to accompany small intensity changes, and this was especially prominent

among blue-shifting spectra, which - as described above - was the typical direction for spectral shift over the course of photobleaching. Intensity change with individual photobleaching events has been interpreted within the domain-limited model of exciton diffusion as a proxy for domain size^{15,37,38}. The data suggests that small domains tend to be spectrally distinct from larger domains, which in turn suggests particular intrachain conformational properties or defects exist that create relatively small, localized, low energy domains.

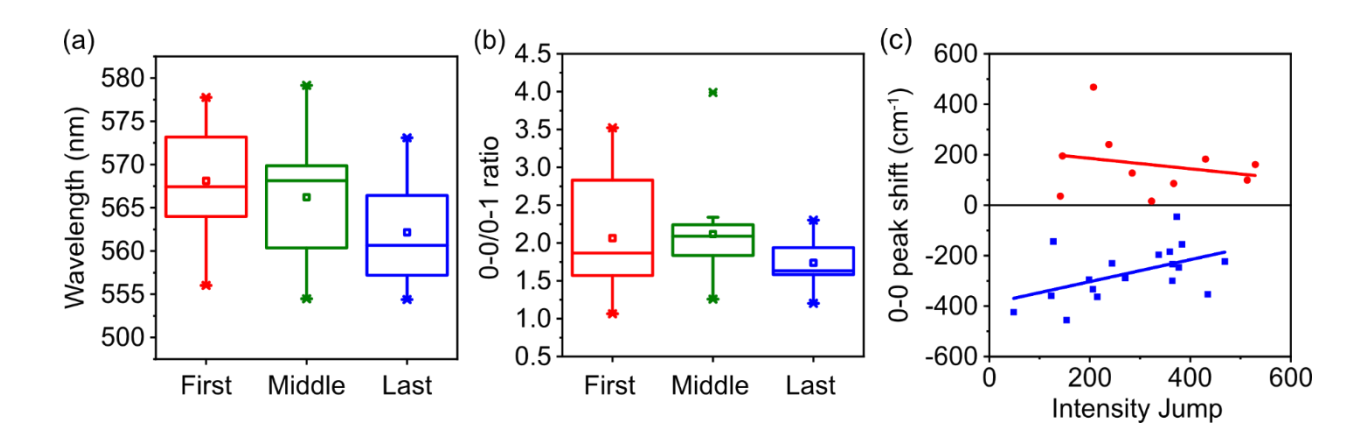


Figure 3. Analysis of photophysical properties of MEH-PPV features with few emitters. (a) Peak position of the 0-0 vibronic peak for identified emitters following spectral SHRImP. (b) Peak height ratio of the 0-0/0-1 vibronic peak for identified emitters following spectral SHRImP. In (a) and (b), n = 13 for first emitter to photobleach, n = 14 for second emitter to photobleach, and n = 14 for last emitter to photobleach. Box plots show line at the median, box ranging from 25^{th} to 75^{th} percentile and whiskers ranging from the 5^{th} to 95^{th} percentile. Small squares indicate mean values. Crosses indicate minimum and maximum values. (c) Correlation between spectral shift of the 0-0 peak and intensity change associated with a photobleaching event, with the spectral difference of an emitter relative to the previously photobleached emitter shown as either red (red-shifted) or blue (blue-shifted) points. Linear fits are included as guides to the eye.

Case Study 2: MEH-PPV Feature with a Complex Intensity Trajectory

Next, we introduce the spatial and spectral subtraction-based super-resolution technique to an MEH-PPV feature displaying a more complex intensity trajectory that shows evidence of a greater number of emitting sites and non-monotonic change in emission intensity (Fig. 4). To determine sections in this more complicated trajectory, STaSI was used to identify intensity changes. From

this analysis, five sections were identified (S1 – S5), with one of those sections (S4) with intensity similar to the background level. Thus, we consider S1, S2, S3, and S5 to contain information on one or more emitting sites. Evaluating spectra after averaging within each of these sections, again reveals a general blue-shift as a function of time; the 0-0 and 0-1 peaks monotonically evolve from 562.0 and 597.6 nm in S1 to 556.6 nm and 588.7 nm in S5, respectively, though without a clear trend in peak height ratio as a function of time.

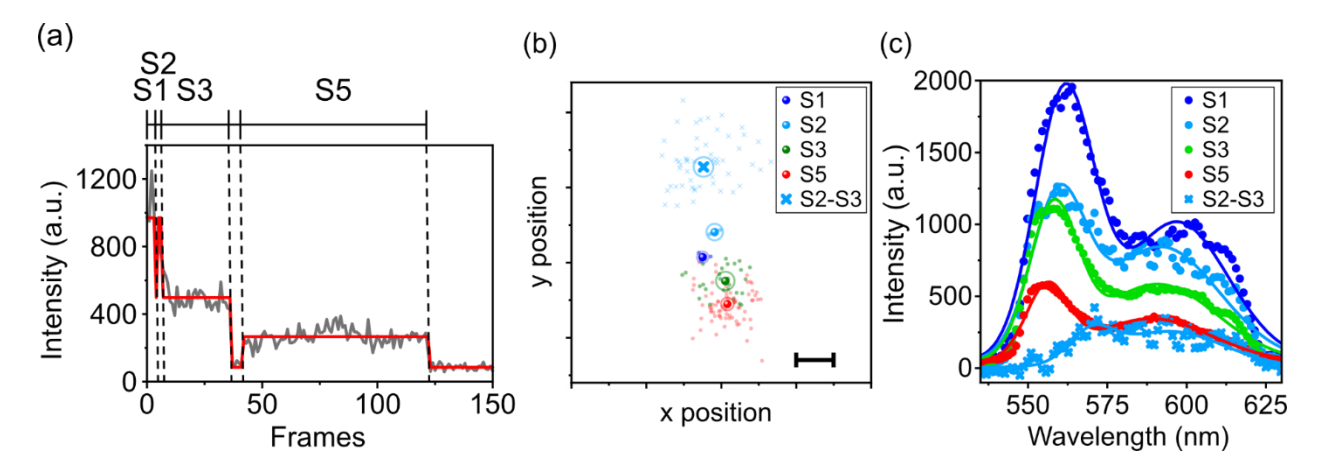


Figure 4. Case study of an MEH-PPV aggregate with a complex intensity trajectory. (a) Fluorescence intensity trajectory shows non-monotonic decay with analyzed sections, as identified by STaSI, labeled S1, S2, S3, and S5. S4 is not labeled because the intensity is near background level. Red line indicates intensity as identified by STaSI. (b) Frame-by-frame localizations (small points) and weight-averaged localizations of the imaged feature present in S1, S2, S3, and S5 (large points) as well as bleached emitter position determined by the subtraction of S3 from S2 using afSHRImP (cross). Circles show the standard error of positions identified through frame-by-frame localizations and afSHRImP. Scale bar: 22.5 nm. (c) Spectra obtained by averaging all spectra collected during the corresponding sections. Subtraction spectrum is obtained by subtracting the S3 spectrum from the S2 spectrum. Solid lines represent best fit curves to two Gaussian functions.

Applying afSHRImP constraints along the full trajectory revealed the same sections identified by STaSI excepting S1 and S2, for which no afSHRImP pairs met the eccentricity and localization uncertainty constraints. Despite this, comparing localization imaging and spectra from S1 and S2 suggests both a spatial and spectral distinction between these sections. A possible explanation is that the same set of chromophores is emitting over S1 and S2 but the relative

intensity is somewhat different, as could result from subtle physical and photophysical changes occurring in the sample: for example, relaxations of either the polymer host or the MEH-PPV may result in subtle changes in torsion in the MEH-PPV, creating slight changes in emission intensity and spectra for each emitter active during this time. Performing a spectral subtraction between S2 and S1 shows a 0-0 peak in similar position but a red-shifted 0-1 peak relative to the spectrum associated with S1 (Fig. S10). This behavior is similar to that shown by MEH-PPV molecules dispersed in a polymeric matrix and thermally annealed at temperatures below the glass transition temperature of the matrix³². In both our experiment and the one described in Reference 32, no significant conformational change is expected in the matrix or the MEH-PPV molecules, yet subtle spectral changes occur. In the case presented here, the likely origin is that upon photobleaching of a particular emitting site, the exciton migration path is altered and (given the consistent blue-shift of the emission in MEH-PPV molecules and aggregates upon photoexposure) involves less interchain exciton transport than supported by the aggregate before partial photodegradation.

For those sections where STaSI identifies a change in intensity and afSHRImP subtractions suggest a change in emitter position, spatial and spectral subtractions were performed. These subtractions show a spectrally and spatially distinct emitter that photobleaches between S2 and S3 (Fig. 4, Fig. S10). This emitter is at a notable physical distance from other identified features and has a distinct spectrum made obvious only when the subtraction is performed. In particular, this emitter is red-shifted relative to other spectra identified in either the simple systems represented by the data in Figs. 2 and 3 or the more complex example examined here. Additionally, the peak height ratio is lower than that associated with any other identified emitter in this study, with a strongly suppressed 0-0 transition, as is typically associated with H-aggregates^{39,40}.

Data present in Sections 3-5 can be explained via multiple pictures that cannot be neatly discriminated even with the spatial and spectral information afforded through the approach described here. One possibility is that S3 contains a single emitter that photobleaches (S4) after which another is photoactivated (S5). It is possible that the emitter associated with S5 is also emitting during S1 and/or S2 and was in a dark state for a portion of the trajectory. Other possibilities include that S3 contains 2 emitting chromophores, one of which is also active in S5 or that the same emitter is on in S3 and S5 but emitting with different intensity, as is suggested for the emitter(s) present in S1 and S2. Localization imaging finds distinct positions for emission in S3 and S5, and the spectra associated with S3 and S5 are nearly identical in peak positions but somewhat different in peak height ratio (Fig. 4, Fig. S10). These factors suggest the last two possibilities are the most likely but do not preclude other possibilities described above.

The two models that have commonly been used to explain exciton migration in MEH-PPV single molecules and aggregates are chain-limited and domain-limited exciton migration: the former assumes exciton migration occurs over the full polymer or aggregate and the latter assumes excitons migrate within particular domains bearing only a single emitting site and between which exciton transfer does not occur^{13,37}. It is generally accepted that aspects of both types of behavior are at play within conjugated polymers and aggregates thereof, with a likelihood that there are particular domains between which exciton migration does not occur but also domains in which more than one emitting site may be present and within which excitons may diffuse. In the representative aggregate explored here, behaviors consistent with a range of exciton migration are present: the large spatial and spectral difference found between the emitter that turns off between Sections 2 and 3 and other emitters suggests emission that is emerging from two distinct domains,

while the emitters represented by Sections 1 and 2 and Sections 3 and 5 may represent exciton migration within a particular domain.

Case Study 3: pPDI Aggregates with Complex Energetic Behavior

For characterizing and validating aspects of the technique used in this study, single molecules of pPDI were employed. Such molecules were also subjected to solvent vapor swelling to form small aggregates as described in Experimental Details, and their fluorescence was collected in the zerothand first-order channels. Unlike for MEH-PPV aggregates, no previous measurements on pPDI are available to guide estimation of and validate pPDI aggregate size and shape, but initial concentration and swelling conditions together with results on MEH-PPV suggest aggregates will consist of fewer than 40 single molecules. As for the MEH-PPV aggregate with complex photophysics described above, for pPDI aggregates sectioning of intensity trajectories were performed via STaSI. The aggregates generally had spectra very similar to single molecules, with average spectra of the single molecules showing nearly identical peak positions but a somewhat larger 0-0/0-1 peak height ratio than the aggregates (Fig. S11). Figure 5 shows two representative cases for pPDI aggregates, each of which shows a complex intensity trajectory and evidence of multiple distinct emitters. Of 16 aggregates examined, 14 showed spectral behavior similar to that shown in Fig. 5c. Here, a pPDI aggregate displays a small degree of spectral blue shift near the 575 nm peak over the course of the trajectory, behavior similar to that seen in MEH-PPV aggregates. We note that the spectral shift (from 575.9 to 572.9 nm) from S1 to S5 is a greater shift than is seen in single molecules over a similar number of frames (Fig. S4b), even in this aggregate with higher intensity and thus lower uncertainty in spectral peak position. The weight-averaged positions identified through localization imaging suggests emission emanating from different locations on the aggregate over the course of the trajectory, with a particular distinction between

the location of emission during the latter sections (S5, S6) relative to the earlier ones. Performing spatial and spectral subtractions between S1 and S5 and S3 and S5 reveal similar locations and very similar spectra, suggesting the emission in S1 and S3 comes from the same emitters. The subtraction spectrum shows that the emitter that photobleaches between Section 3 and Section 5 is red-shifted and has somewhat different vibronic band character compared with the monomer, presumably due to some degree of exciton delocalization over the original aggregate, consistent with Reference 41, where some linear molecules consisting of multiple core PDI units show consecutive bleaching behavior of this type⁴¹. We suggest that adjacent pPDI molecules are weakly coupled in this aggregate (as well as in most aggregates examined) and thus have emission characteristics similar to isolated single molecules.

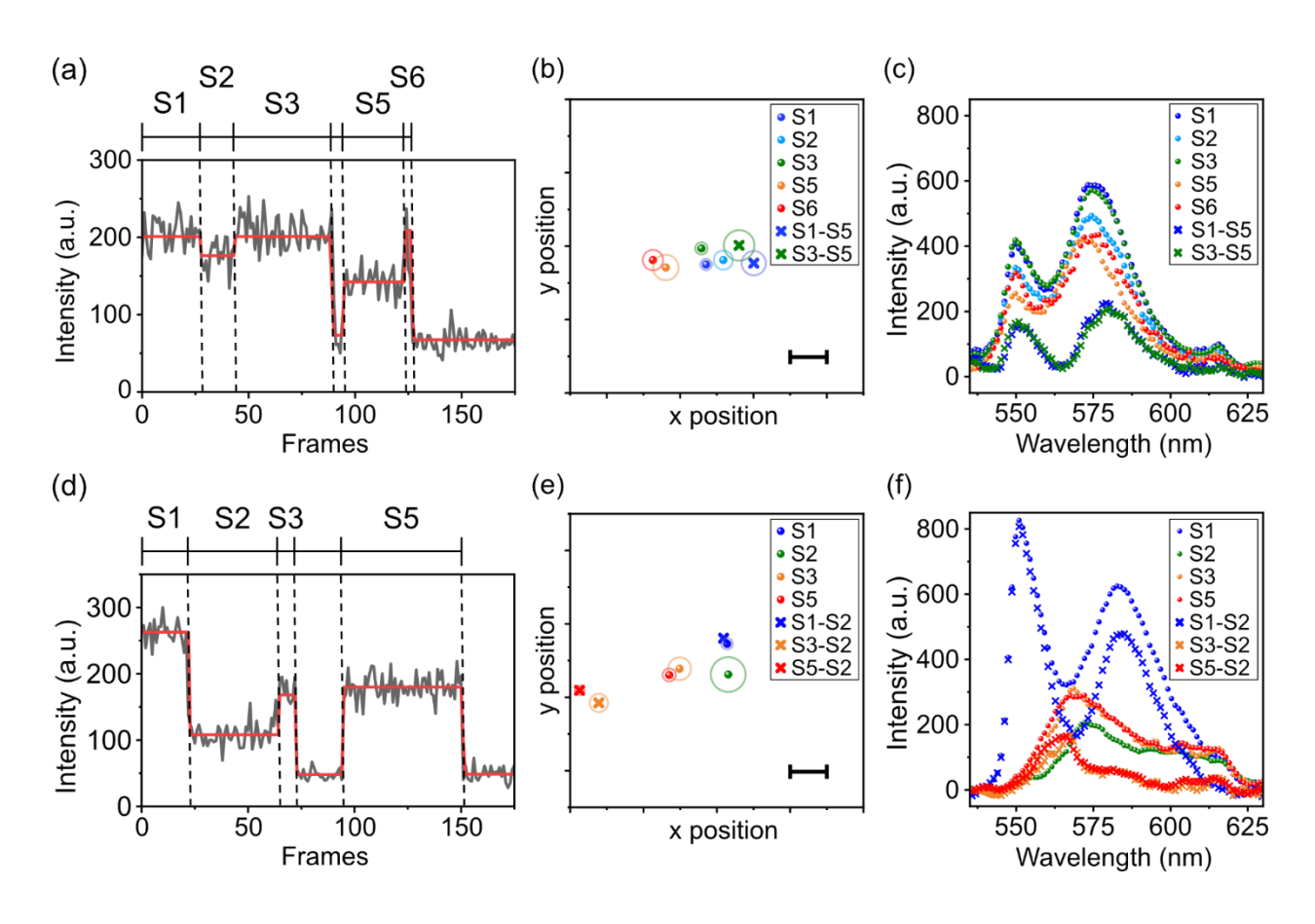


Figure 5. Case study of two pPDI aggregates with complex intensity trajectories. (a) Fluorescence intensity trajectory shows non-monotonic decay with analyzed sections, as identified by STaSI, labeled S1, S2, S3, S5, and S6. S4 is not labeled because the intensity is at background level. Red line indicates intensity as identified by STaSI. (b) Weight-averaged localizations of the imaged feature present in S1, S2, S3, S5, and S6 as well as bleached emitter position determined by the subtraction of S5 from S3 and S5 from S1 using afSHRImP. (c) Spectra obtained by averaging all spectra collected during corresponding sections excepting S4. Subtraction spectrum is obtained by subtracting the S2 spectrum from the S3 spectrum. (d) Fluorescence intensity trajectory shows non-monotonic decay with analyzed sections, as identified by STaSI, labeled S1, S2, S3, and S5. S4 is not labeled because the intensity is at background level. (e) Weight-averaged localizations of the imaged feature present in S1, S2, S3, and S5 as well as bleached emitter position determined by the subtraction of S2 from S1, S3, and S5 using afSHRImP. (f) Spectra obtained by averaging all spectra collected during corresponding sections excepting S4. Subtraction spectrum is obtained by subtracting the S2 spectrum from the S1, S3, and S5 spectra. In b and e, circles show the standard error of positions identified through frame-by-frame localizations in particular sections and by afSHRImP. If no circle is present, standard error is smaller than the symbol. Scale bar: 11.25 nm.

In contrast to the case described above, occasionally cases such as that shown in Fig. 5d-f were observed. In S1, the spectrum is similar to that in the case shown in Fig. 5a-c and to that of single molecules. At the intensity transition that separates S1 and S2, there is an abrupt and stark spectral change, with the spectrum shifting from one quite similar to the that of a single pPDI molecule to one with a peak at ~ 575 nm and a broader peak to the red. Of the 16 aggregates examined, two showed a spectral pattern with this character, with the second showing a clear vibronic progression with peaks at ~570 and 610 nm. For the aggregate shown in Fig. 5d-f, the spectrum evident in S2 shifts to the blue and the feature position shifts as the intensity increases in S3 before returning to background level and then increasing again to a level similar to that in S3 in S5, with a near identical position and spectrum to that in S3. Supposing that the spectrum associated with S1 consists of the sum of the two emitting units, spectral subtraction reveals that the spectrum associated with the first photobleached emitter is single molecule in character. The spectrum associated with the emitter or emitters remaining after S1 exhibits distinct characteristics,

showing 2 red-lying bands with relatively low intensity. As described in Reference 42, π -stacking in PDI derivatives can induce large spectral shifts, and the spectral changes seen are similar to those associated with H-aggregates, though the presence of Hj or hJ aggregates is also possible^{42–44}. Taken together, it appears there are at least two emitting units in this aggregate, one that has single molecule character that is weakly coupled to one or more units having distinctly different character associated with strong electronic coupling. Evaluating the temperature-dependent behavior of such an aggregate could clarify the nature of the coupling⁴⁴.

Beyond the case studies shown in Fig. 5, pPDI aggregates were also assessed for correlations between spatial and spectral measures. As for MEH-PPV (Fig. 3c), the most robust correlation was found between intensity change (a marker of domain size) and 0-1 spectral shift upon photobleaching events (Fig. S12). Like in MEH-PPV aggregates, the emitters associated with lower energy peaks (those that lead to blue-shifted spectra upon photobleaching events) are associated with small changes in intensity, suggesting the presence of small, localized domains with particularly low energy. Again, the effect is seen more strongly in features that have been subjected to the subtraction-based techniques than in those that have been tracked temporally but without subtractions. In contrast, for pPDI aggregates the emitters associated with red shifts upon photobleach show a positive correlation between intensity change and degree of spectral shift. This difference appears to be driven in part by the few cases (as shown in Fig. 5d-f) in which a very large spectral shift occurs and evidence of strong electronic coupling is present.

Conclusion

In this study, we demonstrate super-resolution imaging that employs subtractions in both the spatial and spectral domains enabled by inherent photophysical events such as photoblinking,

photobleaching, and photoactivation of emitters in multi-chromophoric systems that do not extend beyond the diffraction limit. Unlike typical methods that capture photophysical properties averaged over all emitters present, this dual subtraction-based approach reveals the positions and spectra associated with individual emitters within these systems. Using this technique to identify positions of and spectra associated with exciton recombination events in small MEH-PPV aggregates reveals that photobleaching occurs earlier in low energy emission sites than in higher energy ones. This spectral evolution over time sometimes but not always is accompanied by significant emitter position change: when limited position change is present, this suggests withindomain changes to the exciton migration pathway that occurs during photodegradation of the system; in contrast, when larger spatial displacements are present upon photophysical event, this suggests the presence of distinct domains consistent with the domain-limited exciton migration model. Correlation between measures of spatial and spectral change were relatively weak in the systems considered except for change of intensity and spectral peak position upon photobleaching event, indicating the association of small domains with distinct spectra, a correlation that was made readily apparent upon using the dual spatial and spectral subtraction-based technique described here. Applying the multi-modal technique to small aggregates of a perylene diimide derivative also revealed that these aggregates were heterogeneous, with some consisting of individual subunits with distinct spectral characteristics and electronic coupling properties. Through a series of case studies, our findings demonstrate that the spatial-spectral subtraction-based superresolution technique described here can be used to directly probe properties of individual emitters and correlations between those emitters within a diffraction limited spot in complex multichromophoric systems.

Associated Content

The Supporting Information is available free of charge at xxx. Figures show information on spectral calibration and precision as obtained from Tetrabeads, localization error in single pPDI molecules, drift assessment, apparent spectral heterogeneity and precision of single pPDI molecules, contour plots of fit uncertainties and eccentricities associated with afSHRImP fits for a representative feature, localization error in MEH-PPV and pPDI aggregates, correlation between spectral and spatial information in MEH-PPV features, correlation between spectral and intensity information in MEH-PPV aggregate with a complex intensity trajectory, normalized average spectra of pPDI aggregates and single molecules, and correlation between spectral and intensity information in pPDI features. (PDF)

Author Contributions

H.K., Y.K, and L.J.K initiated the project and designed experiments; H.K. performed the experiments; H.K., Y.K., H.Y., and A.J.D. developed code for data analysis and analyzed data. H.K. and L.J.K. interpreted the results; H.K. and L.J.K. wrote the manuscript with review and editing by Y.K., H.Y., and A.J.D; L.J.K. guided the project.

Acknowledgements

This study was supported by the National Science Foundation (CHE 1807931).

References

- (1) Barbara, P. F.; Gesquiere, A. J.; Park, S.-J.; Lee, Y. J. Single-Molecule Spectroscopy of Conjugated Polymers. *Acc. Chem. Res.* **2005**, *38*, 602–610.
- (2) Coceancigh, H.; Higgins, D. A.; Ito, T. Optical Microscopic Techniques for Synthetic Polymer Characterization. *Anal. Chem.* **2019**, *91*, 405–424.
- (3) Feng, J.; Deschout, H.; Caneva, S.; Hofmann, S.; Lončarić, I.; Lazić, P.; Radenovic, A. Imaging of Optically Active Defects with Nanometer Resolution. *Nano Lett.* **2018**, *18*, 1739–1744.
- (4) Comtet, J.; Glushkov, E.; Navikas, V.; Feng, J.; Babenko, V.; Hofmann, S.; Watanabe, K.; Taniguchi, T.; Radenovic, A. Wide-Field Spectral Super-Resolution Mapping of Optically Active Defects in Hexagonal Boron Nitride. *Nano Lett.* **2019**, *19*, 2516–2523.
- (5) Bolinger, J. C.; Traub, M. C.; Brazard, J.; Adachi, T.; Barbara, P. F.; Vanden Bout, D. A. Conformation and Energy Transfer in Single Conjugated Polymers. *Acc. Chem. Res.* **2012**, *45*, 1992–2001.
- (6) Mirzov, O.; Bloem, R.; Hania, P. R.; Thomsson, D.; Lin, H.; Scheblykin, I. G. Polarization Portraits of Single Multichromophoric Systems: Visualizing Conformation and Energy Transfer. *Small* **2009**, *5*, 1877–1888.
- (7) Hou, L.; Adhikari, S.; Tian, Y.; Scheblykin, I. G.; Orrit, M. Absorption and Quantum Yield of Single Conjugated Polymer Poly[2-Methoxy-5-(2-Ethylhexyloxy)-1,4-Phenylenevinylene] (MEH-PPV) Molecules. *Nano Lett.* **2017**, *17*, 1575–1581.
- (8) Thompson, B. C.; Fréchet, J. M. J. Polymer–Fullerene Composite Solar Cells. *Angew. Chemie Int. Ed.* **2008**, *47*, 58–77.
- (9) Moliton, A.; Hiorns, R. C. Review of Electronic and Optical Properties of Semiconductingπ-Conjugated Polymers: Applications in Optoelectronics. *Polym. Int.* **2004**, *53*, 1397–1412.
- (10) Nielsen, C. B.; Holliday, S.; Chen, H.-Y.; Cryer, S. J.; McCulloch, I. Non-Fullerene Electron Acceptors for Use in Organic Solar Cells. *Acc. Chem. Res.* **2015**, *48*, 2803–2812.
- (11) Harrison, N. T.; Baigent, D. R.; Samuel, I. D. W.; Friend, R. H.; Grimsdale, A. C.; Moratti, S. C.; Holmes, A. B. Site-Selective Fluorescence Studies of Poly(p-Phenylene Vinylene) and Its Derivatives. *Phys. Rev. B* **1996**, *53*, 15815–15822.
- (12) Shin, W. S.; Jeong, H.-H.; Kim, M.-K.; Jin, S.-H.; Kim, M.-R.; Lee, J.-K.; Lee, J. W.; Gal, Y.-S. Effects of Functional Groups at Perylene Diimide Derivatives on Organic Photovoltaic Device Application. *J. Mater. Chem.* **2006**, *16*, 384–390.
- (13) Lin, H.; Tabaei, S. R.; Thomsson, D.; Mirzov, O.; Larsson, P.-O.; Scheblykin, I. G. Fluorescence Blinking, Exciton Dynamics, and Energy Transfer Domains in Single Conjugated Polymer Chains. *J. Am. Chem. Soc.* **2008**, *130*, 7042–7051.
- (14) Lin, H.; Hania, P. R.; Bloem, R.; Mirzov, O.; Thomsson, D.; Scheblykin, I. G. Single Chain versus Single Aggregate Spectroscopy of Conjugated Polymers. Where Is the Border? *Phys. Chem. Chem. Phys.* **2010**, *12*, 11770–11777.
- (15) Yang, J.; Park, H.; Kaufman, L. J. Highly Anisotropic Conjugated Polymer Aggregates: Preparation and Quantification of Physical and Optical Anisotropy. *J. Phys. Chem. C* **2017**, *121*, 13854–13862.
- (16) Zhang, F.; Ma, Y.; Chi, Y.; Yu, H.; Li, Y.; Jiang, T.; Wei, X.; Shi, J. Self-Assembly, Optical and Electrical Properties of Perylene Diimide Dyes Bearing Unsymmetrical Substituents at Bay Position. *Sci. Rep.* **2018**, *8*, 8208.
- (17) Usowicz, M. T.; Kelley, M. J.; Singer, K. D.; Duzhko, V. V. Tailored One- and Two-Dimensional Self-Assembly of a Perylene Diimide Derivative in Organic Solvents. *J. Phys. Chem. B* **2011**, *115*, 9703–9709.
- (18) Würthner, F.; Thalacker, C.; Diele, S.; Tschierske, C. Fluorescent J-Type Aggregates and Thermotropic Columnar Mesophases of Perylene Bisimide Dyes. *Chem. A Eur. J.* **2001**, *7*, 2245–2253.
- (19) Simonson, P. D.; Rothenberg, E.; Selvin, P. R. Single-Molecule-Based Super-Resolution Images

- in the Presence of Multiple Fluorophores. Nano Lett. 2011, 11, 5090-5096.
- (20) Wöll, D.; Flors, C. Super-Resolution Fluorescence Imaging for Materials Science. *Small Methods* **2017**, *1*, 1700191.
- (21) Merdasa, A.; Bag, M.; Tian, Y.; Källman, E.; Dobrovolsky, A.; Scheblykin, I. G. Super-Resolution Luminescence Microspectroscopy Reveals the Mechanism of Photoinduced Degradation in CH 3 NH 3 PbI 3 Perovskite Nanocrystals. *J. Phys. Chem. C* **2016**, *120*, 10711–10719.
- (22) Park, H.; Hoang, D. T.; Paeng, K.; Kaufman, L. J. Localizing Exciton Recombination Sites in Conformationally Distinct Single Conjugated Polymers by Super-Resolution Fluorescence Imaging. *ACS Nano* **2015**, *9*, 3151–3158.
- (23) Qu, X.; Wu, D.; Mets, L.; Scherer, N. F. Nanometer-Localized Multiple Single-Molecule Fluorescence Microscopy. *Proc. Natl. Acad. Sci.* **2004**, *101*, 11298–11303.
- (24) Gordon, M. P.; Ha, T.; Selvin, P. R. Single-Molecule High-Resolution Imaging with Photobleaching. *Proc. Natl. Acad. Sci.* **2004**, *101*, 6462–6465.
- (25) Habuchi, S.; Onda, S.; Vacha, M. Mapping the Emitting Sites within a Single Conjugated Polymer Molecule. *Chem. Commun.* **2009**, *32*, 4868.
- (26) Huser, T.; Yan, M.; Rothberg, L. J. Single Chain Spectroscopy of Conformational Dependence of Conjugated Polymer Photophysics. *Proc. Natl. Acad. Sci. U. S. A.* **2000**, *97*, 11187–11191.
- (27) Yu, J.; Hu, D.; Barbara, P. F. Unmasking Electronic Energy Transfer of Conjugated Polymers by Suppression of O2 Quenching. *Science* **2000**, *289*, 1327–1330.
- (28) Jiang, Y.; McNeill, J. Superresolution Mapping of Energy Landscape for Single Charge Carriers in Plastic Semiconductors. *Nat. Commun.* **2018**, *9*, 4314.
- (29) Hoang, D. T.; Yang, J.; Paeng, K.; Kwon, Y.; Kweon, O. S.; Kaufman, L. J. In Situ Multi-Modal Monitoring of Solvent Vapor Swelling in Polymer Thin Films. *Rev. Sci. Instrum.* **2016**, *87*, 015106.
- (30) Thompson, R. E.; Larson, D. R.; Webb, W. W. Precise Nanometer Localization Analysis for Individual Fluorescent Probes. *Biophys. J.* **2002**, *82*, 2775–2783.
- (31) Shuang, B.; Cooper, D.; Taylor, J. N.; Kisley, L.; Chen, J.; Wang, W.; Li, C. B.; Komatsuzaki, T.; Landes, C. F. Fast Step Transition and State Identification (STaSI) for Discrete Single-Molecule Data Analysis. *J. Phys. Chem. Lett.* **2014**, *5*, 3157–3161.
- (32) Ou, J.; Yang, Y.; Lin, W.; Yuan, Z.; Gan, L.; Lin, X.; Chen, X.; Chen, Y. Connection between the Conformation and Emission Properties of Poly[2-Methoxy-5-(2'-Ethyl-Hexyloxy)-1,4-Phenylene Vinylene] Single Molecules during Thermal Annealing. *Appl. Phys. Lett.* **2015**, *106*, 123304.
- (33) Ho, X. L.; Wang, Y.-H.; Chen, P.-J.; Woon, W.-Y.; White, J. D. MEH-PPV Photophysics: Insights from the Influence of a Nearby 2D Quencher. *Nanotechnology* **2019**, *30*, 065702.
- (34) Kwon, Y.; Kaufman, L. J. Nearly Isotropic Conjugated Polymer Aggregates with Efficient Local Exciton Diffusion. *J. Phys. Chem. C* **2019**, *123*, 29418–29426.
- (35) Park, H.; Hoang, D. T.; Paeng, K.; Yang, J.; Kaufman, L. J. Conformation-Dependent Photostability among and within Single Conjugated Polymers. *Nano Lett.* **2015**, *15*, 7604–7609.
- (36) Yu, J.; Hayashi, M.; Lin, S. H.; Liang, K. K.; Hsu, J. H.; Fann, W. S.; Chao, C. I.; Chuang, K. R.; Chen, S. A. Temperature Effect on the Electronic Spectra of Poly(p-Phenylenevinylene). *Synth. Met.* **1996**, *82*, 159–166.
- (37) Habuchi, S.; Onda, S.; Vacha, M. Molecular Weight Dependence of Emission Intensity and Emitting Sites Distribution within Single Conjugated Polymer Molecules. *Phys. Chem. Chem. Phys.* **2011**, *13*, 1743–1753.
- (38) Vogelsang, J.; Adachi, T.; Brazard, J.; Vanden Bout, D. A.; Barbara, P. F. Self-Assembly of Highly Ordered Conjugated Polymer Aggregates with Long-Range Energy Transfer. *Nat. Mater.* **2011**, *10*, 942–946.
- (39) Spano, F. C. The Spectral Signatures of Frenkel Polarons in H- and J-Aggregates. *Acc. Chem. Res.* **2010**, *43*, 429–439.
- (40) Shi, J.; Xu, X.; Xia, Y.; Chen, R.; Hawash, Z.; Deribew, D.; Moons, E.; Inganäs, O.; Scheblykin, I.

- G. Photo-Oxidation Reveals H-Aggregates Hidden in Spin-Cast-Conjugated Polymer Films as Observed by Two-Dimensional Polarization Imaging. *Chem. Mater.* **2019**, *31*, 8927–8936.
- (41) Yoo, H.; Furumaki, S.; Yang, J.; Lee, J.-E.; Chung, H.; Oba, T.; Kobayashi, H.; Rybtchinski, B.; Wilson, T. M.; Wasielewski, M. R.; et al. Excitonic Coupling in Linear and Trefoil Trimer Perylenediimide Molecules Probed by Single-Molecule Spectroscopy. *J. Phys. Chem. B* **2012**, *116*, 12878–12886.
- (42) Fennel, F.; Wolter, S.; Xie, Z.; Plötz, P.-A.; Kühn, O.; Würthner, F.; Lochbrunner, S. Biphasic Self-Assembly Pathways and Size-Dependent Photophysical Properties of Perylene Bisimide Dye Aggregates. *J. Am. Chem. Soc.* **2013**, *135*, 18722–18725.
- (43) Kaufmann, C.; Kim, W.; Nowak-Król, A.; Hong, Y.; Kim, D.; Würthner, F. Ultrafast Exciton Delocalization, Localization, and Excimer Formation Dynamics in a Highly Defined Perylene Bisimide Quadruple π-Stack. *J. Am. Chem. Soc.* **2018**, *140*, 4253–4258.
- Oleson, A.; Zhu, T.; Dunn, I. S.; Bialas, D.; Bai, Y.; Zhang, W.; Dai, M.; Reichman, D. R.; Tempelaar, R.; Huang, L.; et al. Perylene Diimide-Based Hj- and HJ-Aggregates: The Prospect of Exciton Band Shape Engineering in Organic Materials. *J. Phys. Chem. C* **2019**, *123*, 20567–20578.

TOC Graphic

